

Report-Guided Automatic Lesion Annotation for Deep Learning-Based Prostate Cancer Detection in bpmRI

Joeran S. Bosma, Anindo Saha, Matin Hosseinzadeh, Ilse Slootweg, Maarten de Rooij, and Henkjan Huisman

Abstract—Deep learning-based diagnostic performance increases with more annotated data, but manual annotation is a bottleneck in most fields. Experts evaluate diagnostic images during clinical routine, and write their findings in reports. Automatic annotation based on clinical reports could overcome the manual labelling bottleneck. We hypothesise that dense annotations for detection tasks can be generated using model predictions, guided by sparse information from these reports. To demonstrate efficacy, we generated clinically significant prostate cancer (csPCa) annotations, guided by the number of clinically significant findings in the radiology reports. We included 7,756 prostate MRI examinations, of which 3,050 were manually annotated and 4,706 were automatically annotated. We evaluated the automatic annotation quality on the manually annotated subset: our score extraction correctly identified the number of csPCa lesions for 99.3% of the reports and our csPCa segmentation model correctly localised $83.8 \pm 1.1\%$ of the lesions. We evaluated prostate cancer detection performance on 300 exams from an external centre with histopathology-confirmed ground truth. Augmenting the training set with automatically labelled exams improved patient-based diagnostic area under the receiver operating characteristic curve from $88.1 \pm 1.1\%$ to $89.8 \pm 1.0\%$ ($P = 1.2 \cdot 10^{-4}$) and improved lesion-based sensitivity at one false positive per case from $79.2 \pm 2.8\%$ to $85.4 \pm 1.9\%$ ($P < 10^{-4}$), with mean \pm std. over 15 independent runs. This improved performance demonstrates the feasibility of our report-guided automatic annotations. Source code is made publicly available at github.com/DIAGNijmegen/Report-Guided-Annotation. Best csPCa detection algorithm is made available at grand-challenge.org/algorithms/bpmri-cspca-detection-report-guided-annotations/

Index Terms—Automatic annotation, computer-aided detection and diagnosis, magnetic resonance imaging, prostate cancer, report-guided deep learning.

I. INTRODUCTION

Computer-aided diagnosis (CAD) systems in fields where clinical experts are matched or outperformed, typically use

This work was supported, in parts, by Health-Holland (LSHM20103), European Union H2020: ProCAncer-I project (952159), European Union H2020: PANCAIM project (101016851), and Siemens Healthineers (CID: C00225450).

J. S. Bosma, A. Saha, M. Hosseinzadeh, I. Slootweg, M. de Rooij and H. Huisman are with the Diagnostic Image Analysis Group, Radboud University Medical Centre, Nijmegen 6525 GA, The Netherlands (e-mail: {Joeran.Bosma, Anindya.Saha, Matin.Hosseinzadeh, Ilse.Slootweg, Maarten.deRooij, Henkjan.Huisman}@radboudumc.nl)

very large training datasets. Top performing deep learning systems used 29,541 training cases (10,306 patients) for the detection of lung cancer [1], 121,850 training cases (121,850 women) for the detection of breast cancer [2] and 16,114 training cases (12,399 patients) for the classification of skin diseases [3].

Annotation time and cost are major limiting factors, resulting in significantly smaller labelled training datasets in most deep learning fields. In the natural image domain, leveraging samples without target task annotations has proven to be effective, even when manually labelled samples are abundant. On ImageNet, with 1.3 million manually labelled training samples, all eight leaderboard holders of the past three years used additional training samples with automatically generated labels. Several approaches were used: Mahajan *et al.* [4] used 3.5 billion images from Instagram to pre-train their models by predicting the corresponding hashtag (*transfer learning*); Xie *et al.* [5] used a *teacher* model to predict 300 million images scraped from the web and selected 130 million samples to train a new *student* model (*self-training*); and Pham *et al.* [6] pushed the teacher-student approach further by continuously updating the teacher model with reinforcement learning. Although the other five leaderboard holders primarily pursued different research directions, they did incorporate automatic labelling techniques to reach state-of-the-art performance.

In the medical domain, popular techniques to leverage unlabelled samples include transfer learning from a distant or related task, and self-training with automatically generated labels [7]. Other techniques to leverage unlabelled samples include contrastive learning [8]–[10] and self-supervised representation learning [11]. These techniques either pre-train without labels, or directly use model predictions as true labels.

Leveraging clinical information, which is often available in medical reports, to improve training with unlabelled samples is under-explored. Clinical information from reports typically differ from regular training annotations, but can inform the generation of automatic annotations for self-training. One study, Bulten *et al.* [12], generated pixel-level Gleason score annotations in H&E stained prostate biopsies by leveraging pathology reports. First, they generated precise cancer masks. Then, they extracted the Gleason scores from the pathology reports to classify the cancer masks into Gleason grades. These steps allowed the generation of Gleason score annotations in

thousands of prostate biopsies, which would have been infeasible to obtain manually. Incorporating clinical information to guide automatic annotations for self-learning remains to be investigated for medical tasks other than biopsy grading.

We hypothesise that medical detection tasks, where the structure of interest can be counted, can leverage unlabelled cases using report-guided automatic annotations. Specifically, we focus on lesion detection, where each case can have any number of lesions. To demonstrate feasibility of our method, we developed an automatic annotation procedure for clinically significant prostate cancer detection in MRI.

Prostate cancer (PCa) has 1.2 million new cases each year [13], a high incidence-to-mortality ratio and risks associated with treatment and biopsy; making non-invasive diagnosis of clinically significant prostate cancer (csPCa) crucial to reduce both overtreatment and unnecessary (confirmatory) biopsies [14]. Multiparametric MRI (mpMRI) scans interpreted by expert prostate radiologists provide the best non-invasive diagnosis [15], but is a limited resource that cannot be leveraged freely. Computer-aided diagnosis (CAD) can assist radiologists to diagnose csPCa, but present-day solutions lack stand-alone performance comparable to that of expert radiologists [16]–[20].

Datasets used for prostate cancer detection and diagnosis have significantly fewer training samples than datasets used to train top-performing deep learning systems in other medical fields [1]–[3]. Studies tackling csPCa detection in MRI by training on histopathology-confirmed annotations, used datasets with 66–806 (median: 146) samples to train their deep learning system [19]–[26]. Approaches using radiologically-estimated annotations (reported using Prostate Imaging Reporting and Data System: Version 2 (PI-RADS)) used 687–1,736 (median: 1,584) training samples [17], [18], [27]–[29].

Prior work investigated the effect of training set size on prostate cancer detection performance, with radiologically-estimated ground truth for training and testing [18]. This work shows patient-based area under the receiver operating characteristic curve (AUROC) for their internal test set increased logarithmically between 50 and 1,586 training cases, from an AUROC of 79.9% to 87.5%. If this trend continues, tens of thousands of annotated cases would be required to reach expert performance — in concordance with similar applications in medical imaging.

Trained investigators supervised by an experienced radiologist annotated all PI-RADS ≥ 4 findings in more than three thousand of our institutional prostate MRI exams. According to our principal annotator, I.S., she requires about four minutes to annotate a single prostate cancer lesion in 3D. Difficult cases are discussed with radiologists, further increasing the overall duration. Annotating tens of thousands of cases would therefore incur huge costs and an incredibly large time investment.

Our automatic labelling procedure aims to leverage unlabelled cases without any additional manual effort, to use the largest dataset of MRI scans for prostate cancer detection reported in literature to date. We investigate the efficacy of our automatically generated annotations by training csPCa detection models on manually and/or automatically annotated exams. We compare performance of these models to

investigate how automatic annotations compare to manual annotations, and what automatically annotated exams add to manually annotated exams.

The report-guided automatic annotation procedure is presented for csPCa detection in bpMRI using radiology reports. However, the underlying method is neither limited to csPCa, MRI, nor radiology reports, and can be applied universally. Any detection task with countable structures of interest, and clinical information reflecting these findings, can leverage our method to automatically annotate examinations.

II. MATERIALS AND METHODS

A. Datasets

Two datasets with biparametric MRI (bpMRI) scans (axial T2-weighted (T2W), high b-value (≥ 1400) diffusion-weighted imaging (DWI) and apparent diffusion coefficient (ADC) maps) for prostate cancer detection were used.

To train and tune our models, 7,756 studies (6,380 patients) out of 9,275 consecutive studies (7,430 patients) from the Radboud University Medical Centre (RUMC) were included. 1,519 studies were excluded due to incomplete examinations, preprocessing errors, prior treatment, poor scan quality, or a prior positive biopsy (Gleason grade group ≥ 2). All scans were obtained as part of clinical routine and evaluated by at least one of six experienced radiologists (4–25 years of experience). All 1,315 csPCa lesions (PI-RADS ≥ 4) in 3,050 studies between January 2016 and August 2018 were manually delineated by trained investigators (at least 1 year of experience), supervised by an experienced radiologist (M.R., 7 years of experience with prostate MRI).

To test our models, an external dataset of 300 exams (300 patients) from Ziekenhuisgroep Twente (ZGT), acquired between March 2015 and January 2017 was used. All patients in the test set received TRUS biopsies and patients with suspicious findings on MR also received MR-guided biopsies. For 61/300 (20.3%) exams the ground truth was derived from radical prostatectomy, resulting in histopathology-confirmed ground truth for all examinations in the test set.

Further details on patient demographics, study inclusion/exclusion criteria and acquisition parameters can be found in the Supplementary Materials.

B. Automated Segmentation of Report Findings

Radiology reports were used to automatically create voxel-level annotations for csPCa. At a high level, our labelling procedure consists of two steps:

- 1) Count the number of clinically significant findings in each radiology report,
- 2) Localise these findings in their corresponding bpMRI scans with a prostate cancer segmentation model.

A rule-based natural language processing script was developed to automatically extract the PI-RADS scores from radiology reports. The number of clinically significant findings, n_{sig} , is then defined as the number of PI-RADS ≥ 4 findings in an exam. The clinically significant findings are localised by keeping the n_{sig} most confident candidates from a csPCa

segmentation model, as depicted in Fig. 1. These automatically generated voxel-level masks can be used to augment the training dataset and produce new csPCa segmentation models.

1) *Extraction of Report Findings*: Most of the radiology reports in our dataset were generated from a template, and modified to provide additional information. Although multiple templates were used over the years, this resulted in structured reports for most exams. This makes a rule-based natural language processing script a reliable and transparent way to extract PI-RADS scores from our radiology reports.

Simply counting the occurrences of ‘PI-RADS 4/5’ in the report body is reasonably effective, but has some pitfalls. For example, prior PI-RADS scores are often referenced during follow-up exams, resulting in false positive matches. Findings can also be grouped and described jointly, resulting in false negatives. To improve the reliability of the PI-RADS extraction from radiology reports, we extracted the scores in two steps.

First, we tried to split the radiology reports in sections for individual findings. Secondly, we extracted the PI-RADS scores for each section individually. In case the report could not be split in sections per lesion, we applied strict pattern matching on the full report. See the Supplementary Materials for more details. Example report sections are shown in Fig. 2.

2) *Localisation of Report Findings*: To localise csPCa findings in unlabelled bpMRI scans, we employed an ensemble¹ of csPCa segmentation models trained on manually annotated bpMRI scans. From the resulting voxel-level confidence maps we created distinct lesion candidates, as illustrated in Fig. 3. Specifically, we create a lesion candidate by starting at the most confident voxel, and including all connected voxels (in 3D) with at least 40% of the peak’s confidence. After a lesion candidate is extracted, we remove it from the model prediction and continue to the next peak.

Automatic voxel-level csPCa annotations were generated by keeping the n_{sig} most confident lesion candidates, with n_{sig} the number of clinically significant report findings as described in Section II-B.1. If there were fewer lesion candidates than clinically significant report findings, the automatic label is excluded.

C. Models, Preprocessing and Data Augmentation

We have posed the prostate cancer detection task as a voxel-level segmentation task and employed two independent architectures, *nnU-Net* and Dual-Attention U-Net (*DA-UNet*). *nnU-Net* is a self-configuring framework that follows a set of rules to select the appropriate architecture based on the input dataset [30]. The *DA-UNet* architecture was developed specifically for csPCa detection, where it performed best among state-of-the-art architectures [17]. Both are derived from the *U-Net* architecture [31], extended to 3D [32], and use anisotropic pooling or convolutional strides to account for the difference in through-plane and in-plane resolution of prostate MRI. See the Supplementary Materials for more details.

¹Multiple models were ensembled by averaging the softmax confidence maps, which resulted in more consistent segmentation masks compared to a single model. The ensemble also improved localisation of report findings in difficult cases, where a single model was more likely to miss the lesion.

The *nnU-Net* framework typically uses the sum of cross-entropy and soft Dice loss, and applies the loss at multiple resolutions (deep supervision). Motivated by [33] and exploratory experiments, we trained *nnU-Net* using cross-entropy only. Based on prior experience [17], we trained the *DA-UNet* model with Focal Loss ($\alpha = 0.75$) [34].

The acquisition protocol of bpMRI ensures negligible movement between imaging sequences, and little deviation of the prostate from the centre of the scan. Therefore, neither registration between sequences, nor centring of the prostate was deemed necessary. In previous work, we have observed that a centre crop size of $72.0 \text{ mm} \times 72.0 \text{ mm} \times 64.8 \text{ mm}$ at a resampled resolution of $0.5 \text{ mm} \times 0.5 \text{ mm} \times 3.6 \text{ mm/voxel}$ works well for our dataset [17]. To prevent the *nnU-Net* framework to zero-pad these scans, we extended the field of view slightly for this model, to $80.0 \text{ mm} \times 80.0 \text{ mm} \times 72.0 \text{ mm}$ at a resampled resolution of $0.5 \text{ mm} \times 0.5 \text{ mm} \times 3.6 \text{ mm/voxel}$, which corresponds to a matrix size of $160 \times 160 \times 20$.

nnU-Net comes with a predefined data preprocessing and augmentation pipeline, detailed in Supplementary Notes 2.2, 3.2 and 4 of [30]. In short, T2W and DWI scans undergo instance-wise z -score normalisation, while ADC maps undergo robust, global z -score normalisation with respect to the complete training dataset. For our anisotropic dataset, the *nnU-Net* framework applies affine transformations in 2D and applies a wide range of intensity and structure augmentations (Gaussian noise, Gaussian blur, brightness, contrast, simulation of low resolution and gamma augmentation).

For the *DA-UNet* model we used our institutional augmentation pipeline. We perform instance-wise min/max normalisation for T2W and DWI scans. For ADC maps, we divide each scan by 3000 (97.4th percentile), to retain their diagnostically relevant absolute values. Then, we apply Rician noise [35] with $\sigma = 0.01$ to each scan at original resolution, with a probability of 75%. Subsequently, we resample all scans to a uniform resolution of $0.5 \text{ mm} \times 0.5 \text{ mm} \times 3.6 \text{ mm/voxel}$ with bicubic interpolation. Finally, with a probability of 50%, we apply 2D affine data augmentations: horizontal mirroring, rotation with $\theta \sim 7.5 \cdot \mathcal{N}(0, 1)$, horizontal translation with $h_x \sim 0.05 \cdot \mathcal{N}(0, 1)$, vertical translation with $h_y \sim 0.05 \cdot \mathcal{N}(0, 1)$ and zoom with $s_{xy} \sim 1.05 \cdot \mathcal{N}(0, 1)$, where $\mathcal{N}(0, 1)$ is a Gaussian distribution with zero mean and unit variance.

D. Experimental Analysis

1) *Extraction of Report Findings*: Accuracy of automatically counting the number of PI-RADS ≥ 4 lesions in a report (n_{sig}) is determined by comparing against the number of PI-RADS ≥ 4 lesions in the manually annotated RUMC dataset. To account for multifocal lesions (which can be annotated as two distinct regions or a single larger one) and human error in the ground truth annotations, we manually checked the radiology report and verified the number of lesions when there was a mismatch between the ground truth and automatic estimation.

2) *Localisation of Report Findings*: Localisation of clinically significant report findings is evaluated with the sensitivity and average number of false positives per case. Evaluation is performed with 5-fold cross-validation on the labelled RUMC

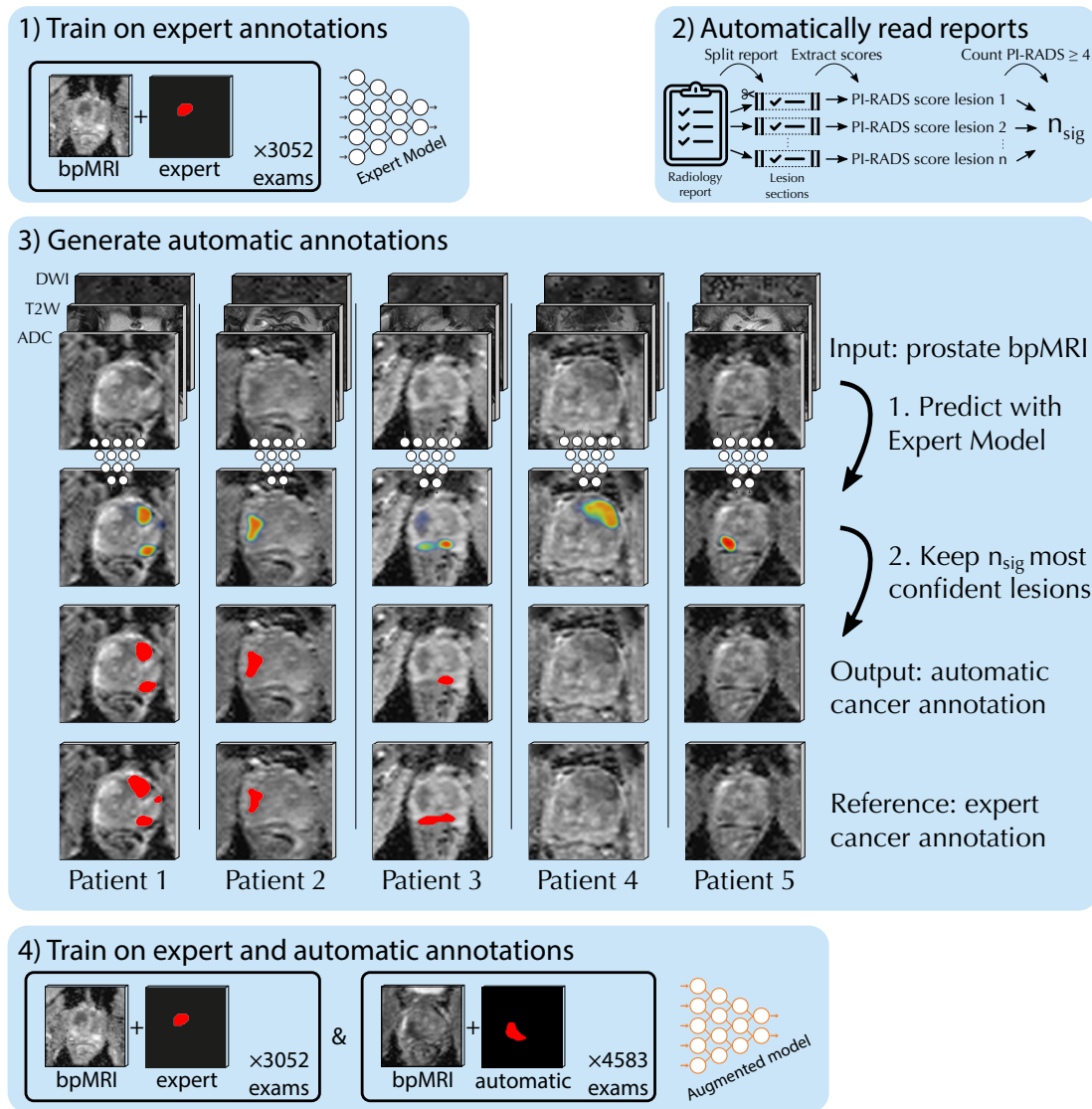


Fig. 1. Overview of the steps to create automatic annotations for the unlabelled RUMC exams. 1) Train a prostate cancer segmentation model on manually annotated clinically significant prostate cancer lesions (csPCa, PI-RADS ≥ 4), the Expert model. 2) Extract the PI-RADS scores from the radiology reports and count the number of csPCa lesions, n_{sig} . 3) Localise and segment the csPCa lesions, by keeping the n_{sig} most confident lesion candidates of the Expert model. 4) Automatic annotations are used to augment the training dataset and train a new prostate cancer segmentation model.

Index lesion mark1: peripheral zone right apex.
T2W/DWI/DCE score: 4/4/+. Minimal ADC value: 821 (normally at least 950). Risk category: intermediate/high-grade cancer (PI-RADS v2 category: 4).

Score extraction → PI-RADS: 4, T2W: 4, DWI: 4, DCE: +

Finding nr. 1: peripheral zone right posterior mid-base prostate. Score T2W: 5, Score DCE: +, Score DWI: 5, minimal ADC value 665. Lesion best fits significant prostate cancer (PI-RADS 5).

Score extraction → PI-RADS: 5, T2W: 5, DWI: 5, DCE: +

Fig. 2. Example lesion report sections. The rule-based score extraction matched the T2W, DWI and DCE scores coloured orange, green and red, respectively. The resulting PI-RADS score is coloured purple. The reports were split in sections by matching the lesion identifier in blue. All reports were originally Dutch.

dataset, for which PI-RADS ≥ 4 lesions were manually annotated in the MRI scan.

3) Segmentation of Report Findings: Quality of the correctly localised report findings is evaluated with the Dice similarity coefficient (DSC). This evaluation is performed with 5-fold cross-validation on the labelled RUMC dataset, which has manual PI-RADS ≥ 4 lesion annotations.

4) Prostate Cancer Detection and Statistical Test: Prostate cancer detection models are evaluated on 300 external exams from ZGT, with histopathology-confirmed ground truth for all patients. Studies are considered positive if they have at least one Gleason grade group ≥ 2 lesion (csPCa) [36]. Patient-based diagnostic performance was evaluated using the Receiver Operating Characteristic (ROC), and summarised

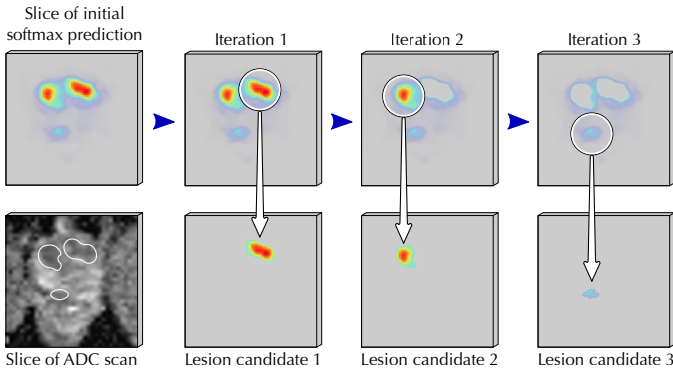


Fig. 3. Depiction of the dynamic lesion candidate selection from a voxel-level prediction. The selected slice shows two high-confidence and one low-confidence lesion candidate extracted from the initial voxel-level prediction. All steps are performed in 3D.

to the area under the ROC curve (AUROC). Lesion-based diagnostic performance was evaluated using Free-Response Receiver Operating Characteristic (FROC), and summarised to the partial area under the FROC curve (pAUC) between 0.01 and 2.50 false positives per case, similar to [17]. We trained our models with 5-fold cross-validation and 3 restarts for *nnU-Net* and 5 restarts for *DA-UNet*, resulting in 15 or 25 independent AUROCs and pAUCs on the test set for each model configuration. To determine the probability of one configuration outperforming another configuration, we performed a permutation test with 100,000 iterations. We used a statistical significance threshold of 0.01.

95% confidence intervals (CI) for the radiologists were determined by bootstrapping 100,000 iterations, with each iteration selecting $\sim \mathcal{U}(0, N)$ samples with replacement and calculating the target metric. Iterations that sampled only one class were rejected.

III. RESULTS

A. Extraction of Report Findings

Our score extraction script correctly identified the number of clinically significant lesions for 3,024 out of the 3,044 (99.3%) radiology reports in our manually labelled RUMC dataset. We excluded reports and their studies when no PI-RADS scores could be extracted from the report: 8 cases (0.3%) from the labelled RUMC dataset and 121 cases (2.6%) from the unlabelled RUMC dataset. Full breakdown of automatically extracted versus manually determined number of significant lesions is given in Fig. 4. Typing mistakes and changed scores in the addendum were the main source of the 20 (0.7%) incorrect extractions, which is an error rate similar to what we observed for our annotators.

B. Localisation of Report Findings

Both prostate cancer segmentation architectures, *nnU-Net* and *DA-UNet*, can achieve high detection sensitivity. At this high sensitivity operating point, the models also propose a large number of false positive lesion candidates, as indicated by the Free-Response Receiver Operating Characteristic (FROC) curve shown in Fig. 5. Masking the models' lesion

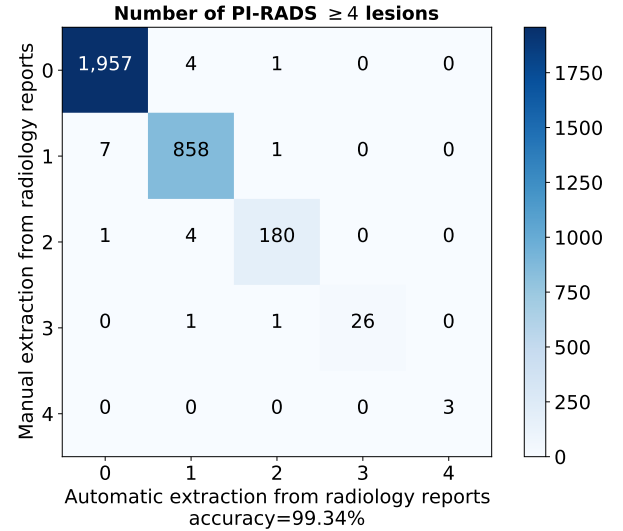


Fig. 4. Confusion matrix for number of clinically significant findings in a radiology report. Evaluated on the labelled RUMC subset.

candidates with the number of clinically significant report findings, n_{sig} , greatly reduces the number of false positive lesion candidates. At the sensitivity of the unfiltered automatic annotations, masking with radiology reports reduced the average number of false positives per case from 0.39 ± 0.14 to 0.064 ± 0.008 for *nnU-Net* and from 0.88 ± 0.29 to 0.097 ± 0.011 for *DA-UNet*. This more than five-fold reduction in false positives greatly increases the usability of the automatic annotations.

Studies where we could extract fewer than n_{sig} lesion candidates were excluded. This excludes studies where we are certain to miss lesions, and thus increases sensitivity. From the automatic annotations from *nnU-Net* we excluded 119 studies, resulting in a sensitivity of $83.8 \pm 1.1\%$ at 0.063 ± 0.008 false positives per study. From the automatic annotations from *DA-UNet* we excluded 4 studies, resulting in a sensitivity of $78.5 \pm 3.3\%$ at 0.096 ± 0.012 false positives per study.

C. Segmentation of Report Findings

Spatial similarity between the automatic and manual annotations is good. *nnU-Net* achieved a Dice similarity coefficient (DSC) of 0.67 ± 0.19 , and *DA-UNet* achieved 0.57 ± 0.17 DSC. Including the missed manual annotations as a DSC of zero, reduces this to 0.51 ± 0.33 for *nnU-Net* and 0.45 ± 0.28 for *DA-UNet*. The full distribution of DSC against lesion volume is given in the Supplementary Materials.

Fig. 1 shows automatic annotations from *nnU-Net*, with a DSC of 0.70 (\approx mean) for the top lesion of Patient 1, a DSC of 0.87 (\approx mean + std.) for Patient 2 and a DSC of 0.55 (\approx mean - std.) for Patient 3.

D. Prostate Cancer Detection

1) *Automatic Labels Compared to Manual Labels*: Training on automatic labels resulted in models with equal or better performance, compared to training on the same number of

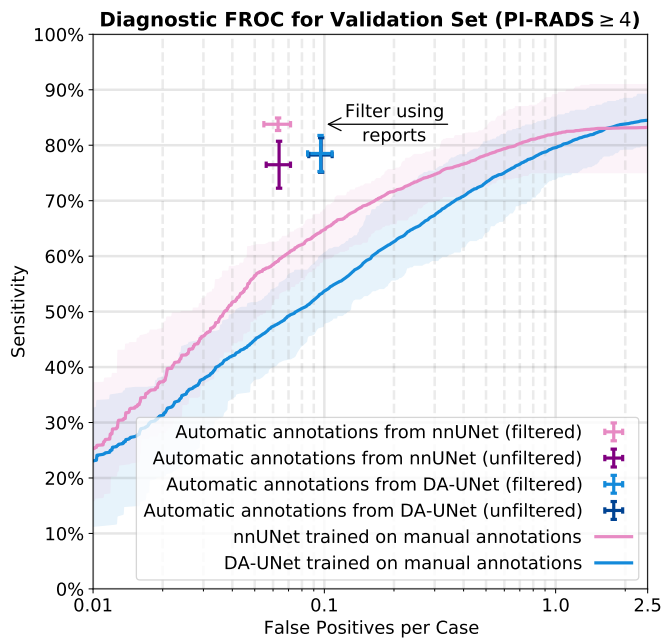


Fig. 5. Free-Response Receiver Operating Characteristic (FROC) curves for matching manually annotated PI-RADS ≥ 4 lesions. Shaded areas indicate the 95% confidence intervals. Masking model predictions with radiology reports significantly improves the false positive rate at high sensitivity, which is the useful range for annotations.

manual labels. For the external test set with histopathology-confirmed ground truth, *nnU-Net* achieved a case-level AUROC of $88.3 \pm 1.1\%$ when training on automatically annotated studies and $88.1 \pm 1.1\%$ when training on manually annotated studies ($P = 0.24$). Training *DA-UNet* on automatically annotated studies resulted in a case-level AUROC of $86.6 \pm 1.4\%$, significantly outperforming training on manually annotated exams, which achieved $84.6 \pm 2.0\%$ AUROC ($P = 4.4 \cdot 10^{-4}$).

Lesion detection performance, as measured by the pAUC, was 1.920 ± 0.036 for *nnU-Net* when training on automatically annotated studies and 1.949 ± 0.056 when training on manually annotated studies ($P = 0.13$). *DA-UNet* trained on automatically annotated exams achieved 2.024 ± 0.039 pAUC, significantly outperforming training on manually annotated exams, which achieved 2.024 ± 0.039 pAUC ($P < 10^{-4}$). Sensitivity at one false positive per case increased from $79.2 \pm 2.8\%$ to $80.4 \pm 2.4\%$ ($P = 0.10$) for *nnU-Net* and from $79.1 \pm 3.6\%$ to $83.5 \pm 1.9\%$ ($P < 10^{-4}$) for *DA-UNet*. See the top row of Fig. 6 for the ROC and FROC curves.

2) Augmenting Training Set with Automatic Annotations:

Augmenting the training set with automatically annotated exams significantly improved model performance. For the external test set with histopathology-confirmed ground truth, the case-level AUROC increased from $88.1 \pm 1.1\%$ to $89.8 \pm 1.0\%$ ($P = 1.2 \cdot 10^{-4}$) for *nnU-Net* and from $84.6 \pm 2.0\%$ to $86.3 \pm 1.8\%$ ($P = 1.8 \cdot 10^{-3}$) for *DA-UNet*.

On this external test set, experienced radiologists had a sensitivity of $91.7 \pm 2.8\%$ at $77.9 \pm 2.9\%$ specificity. At the same sensitivity, adding automatic annotations improved the model's specificity from $60.8 \pm 8.6\%$ to $64.7 \pm 7.1\%$ ($P = 0.35$) for *nnU-Net* and from $38.7 \pm 10.0\%$ to $46.1 \pm 10.5\%$

($P = 7.6 \cdot 10^{-3}$) for *DA-UNet*.

Detection and risk stratification of individual lesions also benefitted from including the automatically labelled training samples. Model performance, as measured by the pAUC, increased from 1.920 ± 0.036 to 2.063 ± 0.036 ($P < 10^{-4}$) for *nnU-Net* and from 1.926 ± 0.080 to 2.008 ± 0.073 ($P = 3.0 \cdot 10^{-4}$) for *DA-UNet*. Sensitivity at one false positive per case increased from $79.2 \pm 2.8\%$ to $85.4 \pm 1.9\%$ ($P < 10^{-4}$) for *nnU-Net* and from $79.1 \pm 3.6\%$ to $82.8 \pm 3.2\%$ ($P = 5.3 \cdot 10^{-4}$) for *DA-UNet*. See the bottom row of Fig. 6 for the ROC and FROC curves.

IV. DISCUSSION AND CONCLUSION

Patient-level risk stratification and lesion-level detection and risk stratification of our prostate cancer detection models significantly improved by augmenting the training set with automatically-generated prostate cancer annotations guided by radiology report findings. This improved performance demonstrates the feasibility of our annotation method. Furthermore, the automatic annotations are of sufficient quality to speed up the manual annotation process, by identifying negative cases that do not need to be looked at, and by providing high quality segmentation masks for the majority of the positive cases.

Our automatic labelling procedure enabled us to utilise thousands of additional prostate MRI exams with radiology reports from clinical routine, without manually annotating each finding in the MRI scan. While automatic annotations reflect the radiologist's findings less accurately compared to human annotators, we found that training exclusively on automatically annotated exams did not lead to statistically inferior model performance, compared to training on an equal number of manual annotations. For *DA-UNet* performance even increased, for both case-level risk stratification and lesion-level detection. We believe the non-inferior or improved performance could be caused by a higher level of consistency in the automatic annotations, compared to the manual annotations. Manual annotations reflect the high inter- and intra-reader variability of PI-RADS ≥ 4 findings [37], [38], while the automatic annotations are generated using a single ensemble of models. Increased consistency could result in a more stable training signal, helping model convergence. The larger improvement of *DA-UNet* compared to *nnU-Net* also raises the question which components caused this difference. Automatic annotations generated using a model trained with Focal Loss ($\alpha = 0.75$) could be better than automatic annotations generated using a model trained with cross-entropy. Or, a model trained with Focal Loss ($\alpha = 0.75$) may benefit more from the increased consistency of automatic annotations. Or, another difference between the training setup of *nnU-Net* and *DA-UNet* causes this difference in performance increase. Further research is necessary to answer these questions, and push performance with automatically annotated exams further.

Augmenting the training dataset with automatically labelled prostate MRI exams consistently improved model performance, with a group of baseline and augmented models truly reflecting the difference in performance due to the automatically labelled exams. Comparing groups of models with a

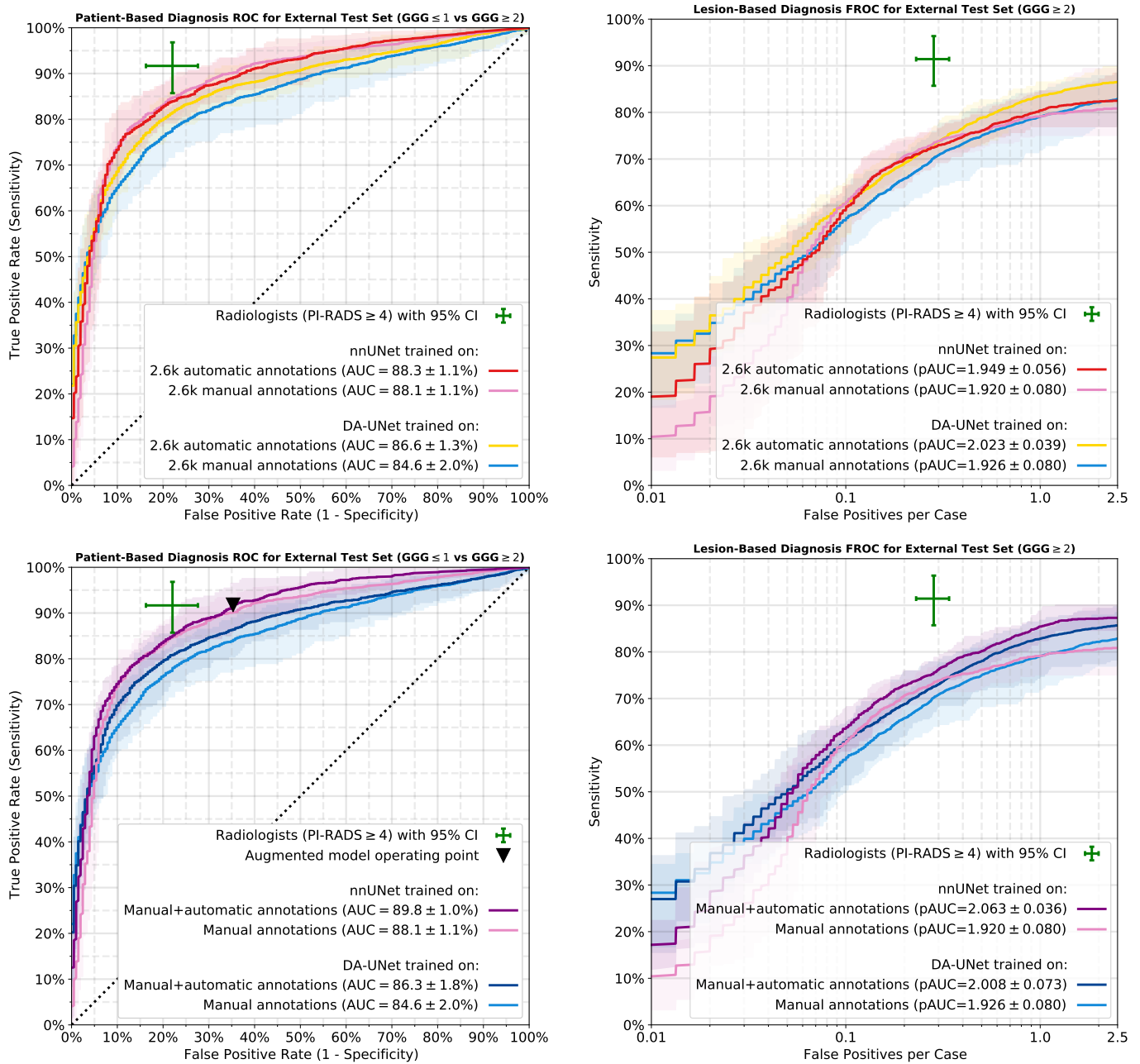


Fig. 6. Model performance for (top row) training on manual PI-RADS ≥ 4 lesion annotations versus the same number of automatic annotations and (bottom row) training on manual annotations versus manual+automatic annotations generated using *nnU-Net* or *DA-UNet*. The (left) panels show ROC curves for patient-based diagnosis of exams with at least one Gleason grade group ($GGG \geq 2$) lesion, and the (right) panels show FROC curves for lesion-based diagnosis of $GGG \geq 2$ lesions. All models are trained on radiology based PI-RADS ≥ 4 annotations and evaluated on the external test set with histopathology-confirmed ground truth. Shaded areas indicate the 95% confidence intervals over 25 restarts.

permutation test ensures results are not due to variation in performance inherent to deep learning’s stochastic nature².

Automatically annotating training samples enables us to improve our models, but also speeds up the manual labelling process for new cases. Accurate PI-RADS score extraction from radiology reports enables us to automatically identify all negative cases (with $\leq 1\%$ error rate), saving the repetitive operation of reading the radiology report only to designate

²Sources of variation include the model’s random initialisation, order of training batches and data augmentations, resulting in differences in model performance between training runs.

a study as negative. As this entails approximately 60% of the studies, this already amounts to a large time saving. Furthermore, the segmentation masks from *nnU-Net* are often of sufficient quality to only require verification of the location, saving significant amounts of time for positive studies as well.

Direct applicability of both the automatic PI-RADS extraction from radiology reports and the models for the automatic annotation procedure are, however, limited. The rule-based score extraction was developed with the report templates from RUMC in mind, and is likely to fail for reports with a different structure. For institutes that also have structured

reports, the rule-based score extraction can be adapted to match their findings. For unstructured (free text) reports, the task of counting the number of clinically significant findings can be performed by a deep learning-based natural language processing model. This model can be trained on the reports of the manually labelled subset, using the number of findings found in the manual annotations as labels.

Another limitation is that the prostate cancer detection models were trained with prostate MRI scans from a single vendor (Siemens Healthineers, Erlangen; Magnetom Trio/Skyra/Prisma/Avanto). Therefore, these models are likely to perform inferior on scans from different scanner models.

In conclusion, the report-guided automatic annotations are of high quality, allowing unlabelled samples to be leveraged without additional manual effort. Furthermore, automatic annotations can speed up the manual annotation process. Our proposed method is widely applicable, paving the way towards larger datasets with equal or reduced annotation time.

V. REFERENCES

- [1] D. Ardila, A. P. Kiraly, S. Bharadwaj, B. Choi, J. J. Reicher, L. Peng, D. Tse, M. Etemadi, W. Ye, G. Corrado, *et al.*, “End-to-end lung cancer screening with three-dimensional deep learning on low-dose chest computed tomography,” *Nature Medicine*, vol. 25, no. 6, pp. 954–961, 2019.
- [2] S. M. McKinney, M. Sieniek, V. Godbole, J. Godwin, N. Antropova, H. Ashrafiyan, T. Back, M. Chesus, G. S. Corrado, A. Darzi, *et al.*, “International evaluation of an AI system for breast cancer screening,” *Nature*, vol. 577, no. 7788, pp. 89–94, 2020.
- [3] Y. Liu, A. Jain, C. Eng, D. H. Way, K. Lee, P. Bui, K. Kanada, G. de Oliveira Marinho, J. Gallegos, S. Gabriele, *et al.*, “A deep learning system for differential diagnosis of skin diseases,” *Nature Medicine*, vol. 26, no. 6, pp. 900–908, 2020.
- [4] D. Mahajan, R. Girshick, V. Ramanathan, K. He, M. Paluri, Y. Li, A. Bharambe, and L. Van Der Maaten, “Exploring the Limits of Weakly Supervised Pretraining,” in *Proceedings of the European Conference on Computer Vision (ECCV)*, 2018, pp. 181–196.
- [5] Q. Xie, M.-T. Luong, E. Hovy, and Q. V. Le, “Self-Training With Noisy Student Improves ImageNet Classification,” in *Proceedings of the IEEE/CVF Conference on Computer Vision and Pattern Recognition*, 2020, pp. 10 687–10 698.
- [6] H. Pham, Z. Dai, Q. Xie, and Q. V. Le, “Meta Pseudo Labels,” in *Proceedings of the IEEE/CVF Conference on Computer Vision and Pattern Recognition (CVPR)*, Jun. 2021, pp. 11 557–11 568.
- [7] V. Cheplygina, M. de Bruijne, and J. P. Pluim, “Not-so-supervised: A survey of semi-supervised, multi-instance, and transfer learning in medical image analysis,” *Medical Image Analysis*, vol. 54, pp. 280–296, 2019.
- [8] K. Chaitanya, E. Erdil, N. Karani, and E. Konukoglu, “Contrastive learning of global and local features for medical image segmentation with limited annotations,” *arXiv preprint arXiv:2006.10511*, 2020.
- [9] H. Sowrirajan, J. Yang, A. Y. Ng, and P. Rajpurkar, “MoCo pretraining improves representation and transferability of chest X-ray models,” in *Medical Imaging with Deep Learning*, PMLR, 2021, pp. 728–744.
- [10] S. Azizi, B. Mustafa, F. Ryan, Z. Beaver, J. Freyberg, J. Deaton, A. Loh, A. Karthikesalingam, S. Kornblith, T. Chen, *et al.*, “Big Self-Supervised Models Advance Medical Image Classification,” *arXiv preprint arXiv:2101.05224*, 2021.
- [11] Z. Zhou, V. Sodha, M. M. R. Siddiquee, R. Feng, N. Tajbakhsh, M. B. Gotway, and J. Liang, “Models Genesis: Generic Autodidactic Models for 3D Medical Image Analysis,” in *International conference on medical image computing and computer-assisted intervention*, Springer, 2019, pp. 384–393.
- [12] W. Bulten, H. Pinckaers, H. van Boven, R. Vink, T. de Bel, B. van Ginneken, J. van der Laak, C. H.-v. de Kaa, and G. Litjens, “Automated Gleason Grading of Prostate Biopsies using Deep Learning,” *arXiv preprint arXiv:1907.07980*, 2019.
- [13] H. Sung, J. Ferlay, R. L. Siegel, M. Laversanne, I. Soerjomataram, A. Jemal, and F. Bray, “Global Cancer Statistics 2020: GLOBOCAN Estimates of Incidence and Mortality Worldwide for 36 Cancers in 185 Countries,” *CA: A Cancer Journal for Clinicians*, vol. 71, no. 3, pp. 209–249, 2021.
- [14] V. Stavrinides, F. Giganti, M. Emberton, and C. M. Moore, “MRI in active surveillance: a critical review,” *Prostate Cancer and Prostatic Diseases*, vol. 22, no. 1, pp. 5–15, 2019.
- [15] D. Eldred-Evans, P. Burak, M. J. Connor, E. Day, M. Evans, F. Fiorentino, M. Gammon, F. Hosking-Jervis, N. Klimowska-Nassar, W. McGuire, *et al.*, “Population-Based Prostate Cancer Screening With Magnetic Resonance Imaging or Ultrasonography: The IP1-PROSTAGRAME Study,” *JAMA Oncology*, 2021.
- [16] R. Cao, X. Zhong, S. Afshari, E. Felker, V. Suvannarerg, T. Tubtawee, S. Vangala, F. Scalzo, S. Raman, and K. Sung, “Performance of Deep Learning and Genitourinary Radiologists in Detection of Prostate Cancer Using 3-T Multiparametric Magnetic Resonance Imaging,” *Journal of Magnetic Resonance Imaging*, 2021.
- [17] A. Saha, M. Hosseinzadeh, and H. Huisman, “End-to-end Prostate Cancer Detection in bPMRI via 3D CNNs: Effects of Attention Mechanisms, Clinical Priori and Decoupled False Positive Reduction,” *Medical Image Analysis*, p. 102 155, 2021, ISSN: 1361-8415.
- [18] M. Hosseinzadeh, A. Saha, P. Brand, I. Sloopweg, M. de Rooij, and H. Huisman, “Deep learning-assisted prostate cancer detection on bi-parametric MRI: minimum training data size requirements and effect of prior knowledge,” *European Radiology*, pp. 1–11, 2021.
- [19] P. Schelb, S. Kohl, J. P. Radtke, M. Wiesenfarth, P. Kickingeder, S. Bickelhaupt, T. A. Kuder, A.

- Stenzinger, M. Hohenfellner, H.-P. Schlemmer, *et al.*, “Classification of Cancer at Prostate MRI: Deep Learning versus Clinical PI-RADS Assessment,” *Radiology*, vol. 293, no. 3, pp. 607–617, 2019.
- [20] A. Seetharaman, I. Bhattacharya, L. C. Chen, C. A. Kunder, W. Shao, S. J. Soerensen, J. B. Wang, N. C. Teslovich, R. E. Fan, P. Ghanouni, *et al.*, “Automated detection of aggressive and indolent prostate cancer on magnetic resonance imaging,” *Medical Physics*, 2021.
- [21] M. Arif, I. G. Schoots, J. C. Tovar, C. H. Bangma, G. P. Krestin, M. J. Roobol, W. Niessen, and J. F. Veenland, “Clinically significant prostate cancer detection and segmentation in low-risk patients using a convolutional neural network on multi-parametric MRI,” *European Radiology*, vol. 30, no. 12, pp. 6582–6592, 2020.
- [22] J. Sanyal, I. Banerjee, L. Hahn, and D. Rubin, “An Automated Two-step Pipeline for Aggressive Prostate Lesion Detection from Multi-parametric MR Sequence,” *AMIA Summits on Translational Science Proceedings*, vol. 2020, p. 552, 2020.
- [23] N. Aldoj, S. Lukas, M. Dewey, and T. Penzkofer, “Semi-automatic classification of prostate cancer on multi-parametric MR imaging using a multi-channel 3D convolutional neural network,” *European radiology*, vol. 30, no. 2, pp. 1243–1253, 2020.
- [24] I. Bhattacharya, A. Seetharaman, W. Shao, R. Sood, C. A. Kunder, R. E. Fan, S. J. C. Soerensen, J. B. Wang, P. Ghanouni, N. C. Teslovich, *et al.*, “CorrSigNet: Learning CORrelated Prostate Cancer SIGnatures from Radiology and Pathology Images for Improved Computer Aided Diagnosis,” in *International Conference on Medical Image Computing and Computer-Assisted Intervention*, Springer, 2020, pp. 315–325.
- [25] R. Cao, A. M. Bajgirani, S. A. Mirak, S. Shakeri, X. Zhong, D. Enzmann, S. Raman, and K. Sung, “Joint Prostate Cancer Detection and Gleason Score Prediction in mp-MRI via FocalNet,” *IEEE transactions on medical imaging*, vol. 38, no. 11, pp. 2496–2506, 2019.
- [26] N. Netzer, C. Weißer, P. Schelb, X. Wang, X. Qin, M. Görtz, V. Schütz, J. P. Radtke, T. Hielscher, C. Schwab, A. Stenzinger, T. A. Kuder, R. Gnirs, M. Hohenfellner, H.-P. Schlemmer, K. H. Maier-Hein, and D. Bonekamp, “Fully Automatic Deep Learning in Bi-institutional Prostate Magnetic Resonance Imaging: Effects of Cohort Size and Heterogeneity,” *Investigative radiology*, 2021.
- [27] T. Sanford, S. A. Harmon, E. B. Turkbey, D. Kessani, S. Tuncer, M. Madariaga, C. Yang, J. Sackett, S. Mehralivand, P. Yan, *et al.*, “Deep-Learning-Based Artificial Intelligence for PI-RADS Classification to Assist Multiparametric Prostate MRI Interpretation: A Development Study,” *Journal of Magnetic Resonance Imaging*, vol. 52, no. 5, pp. 1499–1507, 2020.
- [28] X. Yu, B. Lou, D. Zhang, D. Winkel, N. Arrahmane, M. Diallo, T. Meng, H. von Busch, R. Grimm, B. Kiefer, *et al.*, “Deep Attentive Panoptic Model for Prostate Cancer Detection Using Biparametric MRI Scans,” in *International Conference on Medical Image Computing and Computer-Assisted Intervention*, Springer, 2020, pp. 594–604.
- [29] X. Yu, B. Lou, B. Shi, D. Winkel, N. Arrahmane, M. Diallo, T. Meng, H. von Busch, R. Grimm, B. Kiefer, *et al.*, “False Positive Reduction Using Multiscale Contextual Features for Prostate Cancer Detection in Multi-Parametric MRI Scans,” in *2020 IEEE 17th International Symposium on Biomedical Imaging (ISBI)*, IEEE, 2020, pp. 1355–1359.
- [30] F. Isensee, P. F. Jaeger, S. A. Kohl, J. Petersen, and K. H. Maier-Hein, “nnU-Net: a self-configuring method for deep learning-based biomedical image segmentation,” *Nature Methods*, vol. 18, no. 2, pp. 203–211, 2021.
- [31] O. Ronneberger, P. Fischer, and T. Brox, “U-Net: Convolutional Networks for Biomedical Image Segmentation,” in *International Conference on Medical image computing and computer-assisted intervention*, Springer, 2015, pp. 234–241.
- [32] Ö. Çiçek, A. Abdulkadir, S. S. Lienkamp, T. Brox, and O. Ronneberger, “3D U-Net: Learning Dense Volumetric Segmentation from Sparse Annotation,” in *International Conference on Medical Image Computing and Computer-Assisted Intervention*, Springer, 2016, pp. 424–432.
- [33] M. Baumgartner, P. F. Jaeger, F. Isensee, and K. H. Maier-Hein, “nnDetection: A Self-configuring Method for Medical Object Detection,” *arXiv preprint arXiv:2106.00817*, 2021.
- [34] T.-Y. Lin, P. Goyal, R. Girshick, K. He, and P. Dollár, “Focal Loss for Dense Object Detection,” in *Proceedings of the IEEE International Conference on Computer Vision*, 2017, pp. 2980–2988.
- [35] H. Gudbjartsson and S. Patz, “The Rician distribution of noisy MRI data,” *Magnetic Resonance in Medicine*, vol. 34, no. 6, pp. 910–914, 1995.
- [36] J. I. Epstein, L. Egevad, M. B. Amin, B. Delahunt, J. R. Srigley, and P. A. Humphrey, “The 2014 International Society of Urological Pathology (ISUP) Consensus Conference on Gleason Grading of Prostatic Carcinoma,” *The American Journal of Surgical Pathology*, vol. 40, no. 2, pp. 244–252, 2016.
- [37] A. B. Rosenkrantz, L. A. Ginocchio, D. Cornfeld, A. T. Froemming, R. T. Gupta, B. Turkbey, A. C. Westphalen, J. S. Babb, and D. J. Margolis, “Interobserver Reproducibility of the PI-RADS Version 2 Lexicon: A Multi-center Study of Six Experienced Prostate Radiologists,” *Radiology*, vol. 280, no. 3, pp. 793–804, 2016.
- [38] C. P. Smith, S. A. Harmon, T. Barrett, L. K. Bittencourt, Y. M. Law, H. Shebel, J. Y. An, M. Czarniecki, S. Mehralivand, M. Coskun, *et al.*, “Intra- and interreader reproducibility of PI-RADSv2: A multireader study,” *Journal of Magnetic Resonance Imaging*, vol. 49, no. 6, pp. 1694–1703, 2019.

SUPPLEMENTARY MATERIALS
A. STUDY POPULATION

Table A. Patient demographic and characteristics for datasets acquired at Radboud University Medical Centre (RUMC) and Ziekenhuisgroep Twente (ZGT). Characteristic values are followed by their interquartile range (IQR), if applicable.

Characteristic	RUMC	ZGT
Number of Patients	6,380	300
Number of Studies	7,756	300
• Benign	4,734 [§]	204
• Malignant (≥ 1 csPCa*)	3,022 [§]	96
Median PSA (ng/mL)	8.0 (5 – 11)	6.6 (5 – 9)
Median Age (years)	66 (61 – 70)	65 (59 – 68)
Median Prostate Volume (cm ³)	64 (46 – 91)	50 (40 – 69)
MRI Scanners (3 T, Surface Coils)		
• Magnetom Trio/Skyra ⁺	88.9%	100%
• Magnetom Prisma ⁺	11.0%	–
• Magnetom Avanto ⁺ (1.5 T)	0.1%	–
T2W Acquisition		
• In-Plane Resolution (mm/voxel)	0.30 ± 0.08	0.50 ± 0.00
• Slice Thickness (mm/voxel)	3.60 ± 0.20	3.00 ± 0.00
DWI/ADC Acquisition		
• In-Plane Resolution (mm/voxel)	2.00 ± 0.05	2.00 ± 0.00
• Slice Thickness (mm/voxel)	3.60 ± 0.20	3.00 ± 0.00
• Computed High b-Value	b1400	b1400
MRI-Detected Lesions	10,564 [§]	464
• PI-RADS ≤ 2	5,958 [§]	242
• PI-RADS 3	983 [§]	41
• PI-RADS 4	2,115 [§]	92
• PI-RADS 5	1,508 [§]	89
Histopathology-Confirmed Lesions	N/A	191
• GGG 1 (GS $\leq 3 + 3$)	N/A	86
• GGG 2 (GS 3 + 4)	N/A	50
• GGG 3 (GS 4 + 3)	N/A	24
• GGG 4 (GS 4 + 4)	N/A	9
• GGG 5 (GS $\geq 4 + 5$)	N/A	22

* RUMC csPCa: PI-RADS ≥ 4 ; ZGT csPCa: GGG ≥ 2

⁺ Siemens Healthineers, Erlangen, Germany

[§] Determined semi-automatically

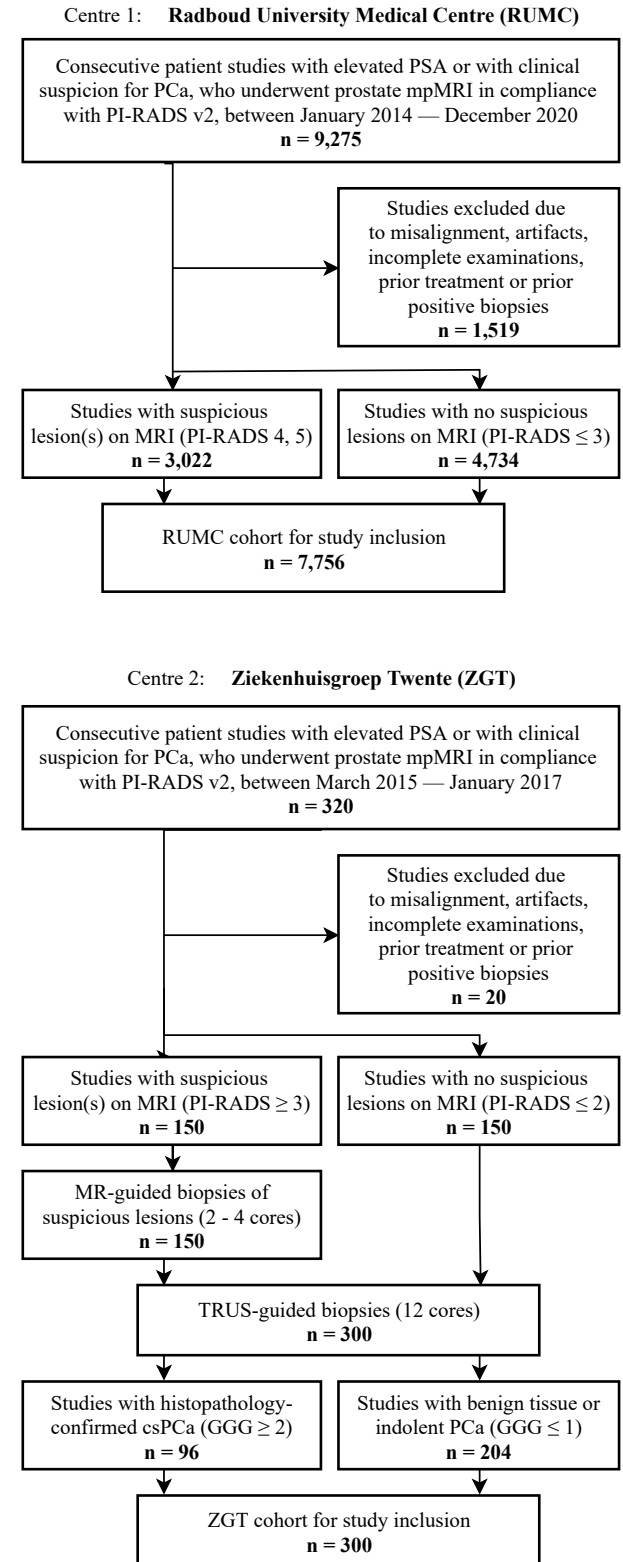


Fig. A. STARD diagram for study inclusion/exclusion criteria applied across both centres: Radboud University Medical Centre (RUMC) and Ziekenhuisgroep Twente (ZGT).

B. EXTRACTION OF REPORT FINDINGS

First, we tried to split the radiology reports in sections for individual findings, by searching for text that matches the following structure:

[Finding] (number indicator) [number]

Where ‘Finding’ matches the Dutch translations ‘*afwijking*’, ‘*laesie*’, ‘*markering*’ or ‘*regio*’. The optional number indicators are ‘*nr.*’, ‘*mark*’ and ‘*nummer*’. The number at the end matches one or multiple numbers (e.g., ‘1’ or ‘2+3’).

Secondly, we extracted the PI-RADS scores by searching for text that matches the following structure:

[PI-RADS] (separators) [number 1-5]

Where the optional separators include ‘*v2 category*’ and ‘*:*’. The dash between ‘*PI*’ and ‘*RADS*’ is optional. The T2W, DWI and DCE scores, which define the PI-RADS score, are extracted analogous to the PI-RADS score, while also allowing joint extraction:

T2W/DWI/DCE score: [1-5]/[1-5]/[-+]

In this instance, the first number is matched with the T2W score, the second with DWI and the + or – with DCE.

In case the report could not be split in sections per lesion, we applied strict pattern matching on the full report. During strict pattern matching we only extract T2W, DWI and DCE scores jointly, to ensure the scores are from the same lesion. The resulting PI-RADS scores were extracted from the full report and matched to the individual scores.

C. DETECTION MODEL ARCHITECTURE

For our prostate cancer segmentation task, *nnU-Net* [1] configured itself to use a 3D *U-Net* with five down-sampling steps, as shown in Fig. B. This figure also shows the specific choice of 2D/3D convolutional blocks, max-pooling layers and transposed convolutions. No cascade of *U-Nets* or 2D *U-Net* was triggered for our dataset.

The implementation of the *DA-U-Net* architecture is the same as in [2], with the exception of *LeakyReLU* [3] activations throughout the decoder and decreased L_2 kernel regularisation of 10^{-4} . See [2] for implementation details.

- [1] F. Isensee, P. F. Jaeger, S. A. Kohl, J. Petersen, and K. H. Maier-Hein, “nnU-Net: a self-configuring method for deep learning-based biomedical image segmentation,” *Nature Methods*, vol. 18, no. 2, pp. 203–211, 2021.
- [2] A. Saha, M. Hosseinzadeh, and H. Huisman, “End-to-end Prostate Cancer Detection in bpMRI via 3D CNNs: Effects of Attention Mechanisms, Clinical Priori and Decoupled False Positive Reduction”, *Medical Image Analysis*, p. 102 155, 2021, ISSN: 1361-8415.
- [3] A. L. Maas, A. Y. Hannun, and A. Y. Ng, “Rectifier Nonlinearities Improve Neural Network Acoustic Models”, in *Proc. icml, Citeseer*, vol. 30, 2013, p. 3.

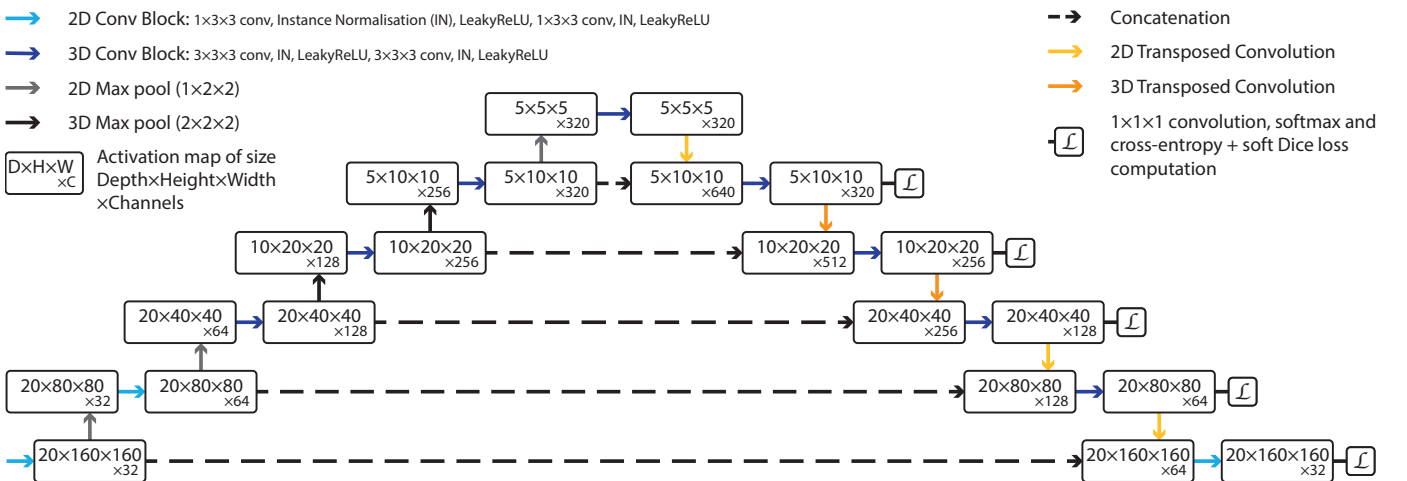


Fig. B. Architecture schematic of the *nnU-Net*, as configured for our prostate cancer segmentation task.

D. LESION SEGMENTATION QUALITY

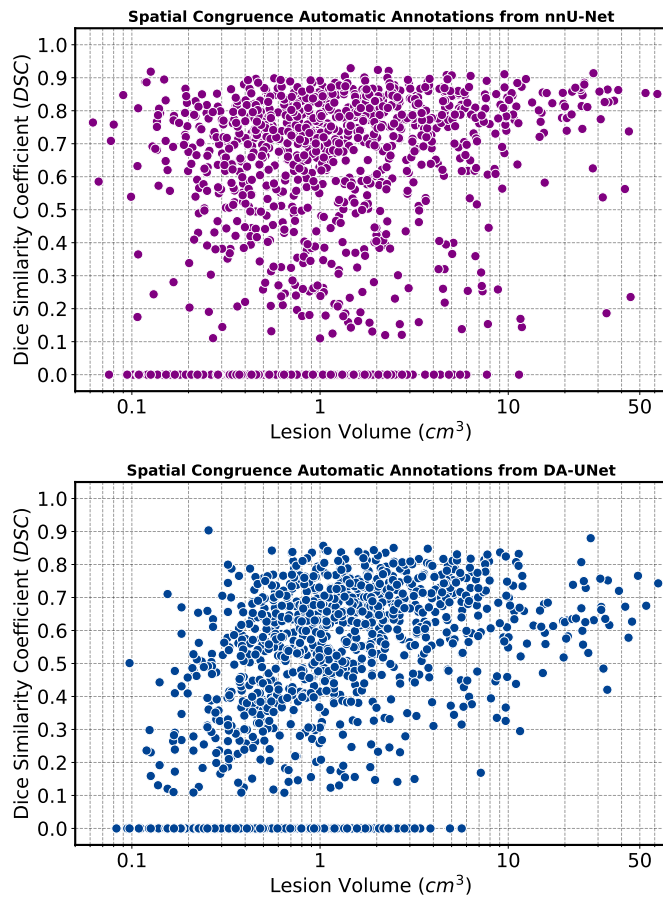


Fig. C. Spatial congruence between automatic and manual csPCa annotations, as measured by the Dice similarity coefficient, for automatic annotations derived from (top) *nnU-Net* or (bottom) *DA-UNet*. Both methods were evaluated on the labelled RUMC dataset with 5-fold cross-validation, excluded studies due to empty PI-RADS extraction from the radiology report, and excluded studies with insufficient lesion candidates. All metrics were computed in 3D.